Progress In Electromagnetics Research B, Vol. 29, 105–138, 2011

A MULTIPLICATIVE REGULARIZED GAUSS-NEWTON ALGORITHM AND ITS APPLICATION TO THE JOINT INVERSION OF INDUCTION LOGGING AND NEAR-BOREHOLE PRESSURE MEASUREMENTS

F. O. Alpak †

Department of Petroleum and Geosystems Engineering
The University of Texas at Austin, USA

T. M. Habashy and A. Abubakar

Schlumberger-Doll Research, USA

C. Torres-Verdín and K. Sepehrnoori

Department of Petroleum and Geosystems Engineering
The University of Texas at Austin, USA

Abstract—Due to the ill-posed nature of nonlinear inverse problems of borehole geophysics, a parameterization approach is necessary when the available measurement data are limited and measurements are only carried out from sparse transmitter-receiver positions (limited data diversity). A potential remedy is the joint inversion of multi-physics measurements. A parametric inversion approach has desirable attributes for multi-physics measurements with different resolutions. It provides a flexible framework to put the sensitivities of multi-physics multi-resolution measurements on equal footing. In addition, the number of unknown model parameters to be inverted is rendered tractable with parameterization. Consequently, a Gauss-Newton based inversion algorithm taking advantage of the Hessian information can be advantageously employed over inversion approaches that rely only on gradient information. We describe a new dual-physics parametric joint-inversion algorithm to estimate near-borehole fluid permeability and porosity distributions of rock formations from fluid-flow and electromagnetic measurements. In order to accommodate the cases in which the measurements are redundant or lack sensitivity with respect

Received 5 September 2010, Accepted 8 March 2011, Scheduled 25 March 2011
Corresponding author: Faruk Omer Alpak (oalpak@yahoo.com).
† Currently with Shell International E&P Inc., USA.

to certain model parameters causing nonuniqueness of the inverted solution, the objective functional to be minimized is regularized with a penalty term. One of the central aspects of this approach is the determination of the regularization parameter. The latter must be chosen in such a way that the relative importance of the misfit between measured and predicted data and the penalty term are effectively balanced over the course of minimization. We propose a new method of adaptively choosing the regularization parameter within a Gauss-Newton method based joint-inversion algorithm using a multiplicative regularization strategy. The multiplicative regularization method is tested against additive regularization in joint-inversion problems involving wireline formation tester transient pressure and induction-frequency electromagnetic logging measurements. The multiplicative regularization method delivers improved convergence rates over additive regularization for all investigated problems. Inversions of relatively more noise-contaminated measurements benefit more from multiplicative regularization.

1. INTRODUCTION

In inverse problems of borehole geophysics, one aims to determine the shape, location, and material property parameters of near-borehole objects from various types of measurements conducted within the borehole. A great majority of borehole geophysical measurements depend on a complex combination of petrophysical and fluid properties of hydrocarbon-bearing formations. This fact renders the family of parameter estimation problems that employ borehole geophysical measurements for inference essentially nonlinear. Such problems call for robust and efficient iterative inversion algorithms.

Physics of multi-phase fluid-flow and electromagnetic induction phenomena in permeable media can be coupled by means of an appropriate saturation equation. Thus, a dual-physics algorithm for the joint inversion of geoelectrical (e.g., induction logging) and flow-related (e.g., wireline formation tester pressure) measurements can be formulated to yield a rigorous estimation of the underlying petrophysical model. Dynamic characteristics of the mud-filtrate invasion phenomenon form the basis for the petrophysical inversion of conductivity profiles around the borehole by employing two-phase fluid-flow physics and geoelectrical modeling. Previous efforts in this subject can be found in [7, 13, 14, 16, 17, 20, 22]. We developed a robust, accurate, and efficient framework for the parametric joint inversion of electromagnetic induction and transient formation pressure measurements. The inversion algorithm yields petrophysical

properties, namely, layer-by-layer horizontal and vertical fluid (also known as absolute) permeabilities, and porosities of hydrocarbon-bearing formations. Inversion of dual-physics measurements is posed as an optimization problem where a quadratic objective functional is minimized subject to physical constraints on the model. An in-depth description of the physical aspects of dual-physics inversion methodology for electromagnetic induction logging and wireline formation tester pressure measurements can be found in [3]. Dual-physics forward modeling and inversion methods that rigorously link electromagnetics and fluid flow have been previously developed, tested, and validated in [24–27].

Including [3], in all of the publications listed above, the physics of coupled flow and electromagnetic induction problem takes priority over the details of the inversion algorithm. Early work, for example, [17] and [20], make use of a less robust history-matching approach rather than full-nonlinear inversion. Others make use of off-the-shelve library routines to perform minimization of a data-mismatch based objective functional, see for instance [16]. We take a rather different route from the mainstream brute-force solution approach to the dual-physics inverse problem at hand. We develop a weighted and regularized Gauss-Newton inversion algorithm from ground-up. The algorithm performs single-physics/single-data-type inversions as well as multi-physics/multi-data-type inversions. It also features a new multiplicative regularization technique, the main focus of the paper.

Characteristically, the number of informative data is not sufficient for constructing accurate high-resolution permeability/porosity images of the near-borehole formation using standard induction logging and wireline formation testing tools. Measurements are acquired only at limited source-receiver positions leading to limited data diversity. Thus, the parameterization of model domain prior to joint inversion is a necessity in order to arrive at a reliable solution. The parameterization process also balances the resolution and volume-of-investigation mismatch between pressure and electromagnetic field measurements. The number of unknown model parameters is rendered manageable via parameterization leading to a non-underdetermined system. A weighted and regularized Gauss-Newton inversion algorithm updates iteratively the model parameters via minimizing the misfit between actual and simulated measurements. It employs a L_2-norm based objective functional. It is important to note that induction logging and formation tester pressure measurements typically contain some noise. Since the updates of model parameters are determined from the data misfit (computed using noisy measurements), one has to be extremely cautious in dealing with the ill-posed nature of the

inverse problem in order to avoid unphysical local minima. Thus, data weighting and optimal regularization are essential components of inversion. In our formulation of the regularization procedure, we are inspired by the work of [1, 9, 18, 19] on the multiplicative regularization of inversion algorithms applied to electromagnetic problems. In this work, we implement the multiplicative regularization technique within the framework of a dual-physics joint-inversion algorithm. We pose the regularization as a multiplicative factor in the objective functional. Computation of the appropriate regularization parameter is controlled by the minimization process itself over the course of inversion iterations.

A two-dimensional axisymmetric petrophysical model is employed for the testing and validation of additive and multiplicative regularization techniques. Estimation of layer-by-layer fluid permeability and porosity values constitutes the objective of joint inversion. Numerically simulated (synthetic) measurements are contaminated by use of various levels of Gaussian random noise. These synthetic measurements are, in turn, used in the proof-of-concept test cases described in this paper. Hereafter, we will refer to the fluid permeability of rock formations simply as permeability in this paper. Examples are presented for various noise levels as well as for a plethora of data-acquisition strategies. A separate test case is provided in which the porous medium exhibits permeability anisotropy. Inversion results are reported along with uncertainty bounds. Efficiency of the additive and multiplicative regularization techniques for joint inversion are compared taking the progress of misfit reduction as the criterion.

2. ADDITIVE REGULARIZATION

We define the vector of residuals $\mathbf{e}(\mathbf{x})$ as a vector whose j-th element is the residual error (also referred to as the data mismatch) of the j-th measurement. The residual error is defined as the difference between the measured and the predicted normalized responses given by

$$\mathbf{e}(\mathbf{x}) = \begin{bmatrix} e_1(\mathbf{x}) \\ \vdots \\ e_M(\mathbf{x}) \end{bmatrix} = \begin{bmatrix} S_1(\mathbf{x}) - m_1 \\ \vdots \\ S_M(\mathbf{x}) - m_M \end{bmatrix} = \mathbf{S}(\mathbf{x}) - \mathbf{m}, \qquad (1)$$

where M is the number of measurements. In Equation (1), m_j is the normalized observed response (measured data) and S_j is corresponding to the normalized simulated response as predicted by the vector of

model parameters, $\mathbf{x}$, given by

$$\mathbf{x} = \begin{bmatrix} x_1 \\ \vdots \\ x_N \end{bmatrix} = \mathbf{y} - \mathbf{y}_R, \tag{2}$$

where N is the number of unknowns. A normalized form of Equation (1) is employed to construct a balanced multi-physics vector of residuals for pressure and magnetic field measurements. We define $\mathbf{e}(\mathbf{x})$ as follows:

$$e_j(\mathbf{x}) = \frac{S_j(\mathbf{x})}{m_j} - 1, \tag{3}$$

and hence

$$\|\mathbf{e}(\mathbf{x})\|^2 = \sum_{j=1}^{M} \left| \frac{S_j(x)}{m_j} - 1 \right|^2. \tag{4}$$

We represent the vector of model parameters $\mathbf{x}$ as the difference between the vector of the actual model parameters $\mathbf{y}$ and a reference model (or background model) $\mathbf{y}_R$. The reference model includes all *a priori* information on the model parameters such as those derived from independent measurements. We first describe a conventional approach to borehole geophysical inversion. The estimation problem is posed as the minimization of an additive objective functional, $C(\mathbf{x})$, given by

$$C(\mathbf{x}) = \frac{1}{2} \left[\left\{ \|\mathbf{W}_d \cdot \mathbf{e}(\mathbf{x})\|^2 - \chi^2 \right\} + \Lambda \|\mathbf{W}_x \cdot (\mathbf{x} - \mathbf{x}_p)\|^2 \right]. \tag{5}$$

The scalar factor Λ ($0 < \Lambda < \infty$) is a Lagrange multiplier (also called regularization parameter or damping coefficient). It is a trade-off parameter determining the relative importance of the two terms of the objective functional. The determination of Λ will produce an estimate of the model $\mathbf{x}$ that has a finite minimum weighted norm (away from a prescribed model $\mathbf{x}_p$) and which globally misfits the data to within a prescribed value χ (determined from *a priori* estimates of the noise level in the data). The second term of the objective functional is included to regularize the minimization problem. It acts as a safeguarding mechanism for the inversion problems in which measurements are redundant or lack sensitivity to certain model parameters causing significant nonuniqueness in the domain of possible solutions. It also suppresses any possible magnification of errors in our parameter estimations due to noise which is unavoidably present in the measurements. These error magnifications may result in undesirable large variations in the model parameters which may cause instabilities in the inversion. In Equation (5), $\mathbf{W}_x^T \mathbf{W}_x$ is the inverse of the

model covariance matrix representing the degree of confidence in the prescribed model $\mathbf{x}_p$. On the other hand, $\mathbf{W}_d^T\mathbf{W}_d$ is the inverse of the data covariance matrix, which describes the estimated uncertainties (due to noise contamination) in the measurements. It describes not only the estimated variance for each particular data point, but also the estimated correlation between errors. $\mathbf{W}_d^T\mathbf{W}_d$ provides a point-by-point weighting of the input data according to a prescribed criterion. Hence, it can be used to reduce the effect of outliers in the data. If the measurement noise is stationary and uncorrelated, then $\mathbf{W}_d = \mathrm{diag}\{\sigma_j\}$ where σ_j is the root-mean-square deviation (standard deviation) of the noise for the j-th measurement.

To solve the nonlinear inverse problem, we employ the Gauss-Newton minimization approach [8] which is based on a local quadratic model of the objective functional. The quadratic model is formed by taking the first three terms of the Taylor series expansion of the objective functional around the current k-th iteration ($\mathbf{x}_k$), as follows:

$$C(\mathbf{x}_k + \mathbf{p}_k) \approx C(\mathbf{x}_k) + \mathbf{g}^T(\mathbf{x}_k) \cdot \mathbf{p}_k + \frac{1}{2}\mathbf{p}_k^T \cdot \mathbf{G}(\mathbf{x}_k) \cdot \mathbf{p}_k, \qquad (6)$$

where the superscript T indicates transposition and $\mathbf{p}_k = \mathbf{x}_{k+1} - \mathbf{x}_k$ is the step in $\mathbf{x}_k$ towards the minimum of the objective functional $C(\mathbf{x})$. The vector $\mathbf{g}(\mathbf{x}) = \nabla C(\mathbf{x})$ is the gradient vector of the objective functional $C(\mathbf{x})$ and described by

$$\mathbf{g}(\mathbf{x}) = \mathbf{J}^T(\mathbf{x}) \cdot \mathbf{W}_d^T \cdot \mathbf{W}_d \cdot \mathbf{e}(\mathbf{x}) + \Lambda \mathbf{W}_x^T \cdot \mathbf{W}_x \cdot (\mathbf{x} - \mathbf{x}_p). \qquad (7)$$

In Equation (7), $\mathbf{J}(\mathbf{x})$ is the $M \times N$ Jacobian matrix, and is given by the following expression:

$$\mathbf{J}(\mathbf{x}) = \begin{bmatrix} \partial S_1/\partial x_1 & \dots & \partial S_1/\partial x_j & \dots & \partial S_1/\partial x_N \\ \vdots & \ddots & \vdots & \ddots & \vdots \\ \partial S_l/\partial x_1 & \dots & \partial S_l/\partial x_j & \dots & \partial S_l/\partial x_N \\ \vdots & \ddots & \vdots & \ddots & \vdots \\ \partial S_M/\partial x_1 & \dots & \partial S_M/\partial x_j & \dots & \partial S_M/\partial x_N \end{bmatrix}. \qquad (8)$$

$\mathbf{G}(\mathbf{x})$ denotes the Gauss-Newton Hessian of the objective functional $C(\mathbf{x})$ which is a real and symmetric $N \times N$ matrix given by

$$\mathbf{G}(\mathbf{x}) = \mathbf{J}^T(\mathbf{x}) \cdot \mathbf{W}_d^T \cdot \mathbf{W}_d \cdot \mathbf{J}(\mathbf{x}) + \Lambda \mathbf{W}_x^T \cdot \mathbf{W}_x \qquad (9)$$

Note that the Gauss-Newton Hessian $\mathbf{G}(\mathbf{x})$ of the objective functional $C(\mathbf{x})$ avoids the expensive computation of second derivatives. As the trade-off, it does not include second-order information that accounts for curvature. The minimum of the right-hand side of Equation (6) is achieved if $\mathbf{p}_k$ is a minimum of the quadratic functional

$$\phi(\mathbf{p}) = \mathbf{g}^T(\mathbf{x}_k) \cdot \mathbf{p} + \frac{1}{2}\mathbf{p}^T \cdot \mathbf{G}(\mathbf{x}_k) \cdot \mathbf{p}. \qquad (10)$$

The functional $\phi(\mathbf{p})$ has a stationary point (a minimum, a maximum or a saddle point also called point of inflection) at $\mathbf{p}_o$, only if the gradient vector of $\phi(\mathbf{p})$ vanishes at $\mathbf{p}_o$, i.e.,

$$\nabla\phi(\mathbf{p}_o) = \mathbf{G} \cdot \mathbf{p}_o + \mathbf{g} = 0. \tag{11}$$

Thus, the stationary point is the solution to the following set of linear equations:

$$\mathbf{G} \cdot \mathbf{p}_o = -\mathbf{g}. \tag{12}$$

Let λ_j and $\mathbf{v}_j$ be the eigenvalues and the corresponding orthonormal eigenvectors of the $N \times N$ real symmetric matrix $\mathbf{G}$

$$\mathbf{G} \cdot \mathbf{v}_j = \lambda_j \mathbf{v}_j, \tag{13}$$

such that

$$\mathbf{v}_i^T \cdot \mathbf{v}_j = \delta_{ij}. \tag{14}$$

The eigenvalues can be computed via

$$\lambda_j = \frac{\mathbf{v}_j^T \cdot \mathbf{G} \cdot \mathbf{v}_j}{\|\mathbf{v}_j\|^2} = \Lambda\|\mathbf{W}_x \cdot \mathbf{v}_j\|^2 + \|\mathbf{W}_d \cdot \mathbf{J} \cdot \mathbf{v}_j\|^2 \geq 0. \tag{15}$$

The inequality of (15) shows that $\mathbf{G}$ is a positive semi-definite matrix. It also indicates that $\mathbf{G}$ can be constructed as a positive-definite matrix by the proper choice of Λ.

The Gauss-Newton search direction $\mathbf{p}_k$ is given by the vector that solves Equation (12). This approach has a rate of convergence that is slightly less than quadratic but significantly better than linear. It provides quadratic convergence in the neighborhood of the minimum. Convergence of the regularized Gauss-Newton inversion method is accelerated by a line-search method [2]. The computational cost per iteration is reduced via adaptive use of Rank-One and Rank-Two approximate update formulas for $\mathbf{G}$, namely, Broyden Symmetric Rank-One update, Powell-Symmetric-Broyden (PSB) update, Davidson-Fletcher-Powell (DFP) update, and Broyden-Fletcher-Goldfarb-Shanno (BFGS) update [8].

3. MULTIPLICATIVE REGULARIZATION

We modify the objective functional given by the Equation (5) as follows:

$$C_k(\mathbf{x}) = F(\mathbf{x})R_k(\mathbf{x}), \tag{16}$$

where $F(\mathbf{x})$ represents the non-regularized objective functional given by

$$F(\mathbf{x}) = \frac{1}{2}\|\mathbf{W}_d \cdot \mathbf{e}(\mathbf{x})\|^2, \tag{17}$$

where k is the iteration count. The regularization factor $R_k(\mathbf{x})$ is chosen to be

$$R_k(\mathbf{x}) = \eta_k \left(\|\mathbf{W}_x \cdot (\mathbf{x} - \mathbf{x}_p)\|^2 + \|\delta\|^2 \right), \tag{18}$$

where

$$\eta_k = \frac{1}{\|\mathbf{W}_x \cdot (\mathbf{x}_k - \mathbf{x}_p)\|^2 + \|\delta\|^2}. \tag{19}$$

δ is a constant determined via numerical experimentation. It is important to note that the regularization is significantly less sensitive to the choice of δ compared to the choice of the Lagrange multiplier Λ. Away from the minimum (in the initial stages of the iterative search), the Gauss-Newton algorithm demands a stronger regularization term to guide the solution closer to the minimum by use of *a priori* information about model characteristics. When the model parameters approach closer to the minimum, it is desirable for the search to be dominated by the misfit term for a more accurate inversion result. Therefore, the intensity of the regularization term needs to be adaptively adjusted in an auditable fashion. The multiplicative technique offers such an adaptive regularization strategy. The normalization in the regularization factor $R_k(\mathbf{x})$ is chosen such that $R_k(\mathbf{x} = \mathbf{x}_k) = 1$ in our implementation, which ensures that the value of the regularization parameter approaches unity at the final stages of the minimization, i.e., $\lim_{k\to\infty} R_k(\mathbf{x}_{k+1}) = 1$.

With multiplicative regularization, the gradient of the objective functional $C(\mathbf{x})$ is given by the following expression:

$$\begin{aligned}\mathbf{g}_k &= \mathbf{g}(\mathbf{x} = \mathbf{x}_k) \\ &= \mathbf{J}^T(\mathbf{x}_k) \cdot \mathbf{W}_d^T \cdot \mathbf{W}_d \cdot \mathbf{e}(\mathbf{x}_k) + \eta_k F(\mathbf{x}_k) \mathbf{W}_x^T \cdot \mathbf{W}_x \cdot (\mathbf{x}_k - \mathbf{x}_p),\end{aligned} \tag{20}$$

and the Gauss-Newton Hessian matrix of the objective functional $C(\mathbf{x})$ is given by

$$\begin{aligned}\mathbf{G}_k &= \mathbf{G}(\mathbf{x} = \mathbf{x}_k) \\ &= \mathbf{J}^T(\mathbf{x}_k) \cdot \mathbf{W}_d^T \cdot \mathbf{W}_d \cdot \mathbf{J}(\mathbf{x}_k) + \eta_k F(\mathbf{x}_k) \mathbf{W}_x^T \cdot \mathbf{W}_x \\ &\quad + \eta_k \left[\mathbf{W}_x^T \cdot \mathbf{W}_x \cdot (\mathbf{x}_k - \mathbf{x}_p) \right]^T \cdot \mathbf{J}^T(\mathbf{x}_k) \cdot \mathbf{W}_d^T \cdot \mathbf{W}_d \cdot \mathbf{e}(\mathbf{x}_k) \\ &\quad + \eta_k \left[\mathbf{J}^T(\mathbf{x}_k) \cdot \mathbf{W}_d^T \cdot \mathbf{W}_d \cdot \mathbf{e}(\mathbf{x}_k) \right]^T \cdot \mathbf{W}_x^T \cdot \mathbf{W}_x \cdot (\mathbf{x}_k - \mathbf{x}_p).\end{aligned} \tag{21}$$

Due to the sparsity of *a priori* information about the underlying model, constructing a reliable $\mathbf{x}_p$ is often not possible for the near-borehole geophysical problems. In order to constrain the minimization process such that the inverted model parameters, $\mathbf{x}_k$, will not exhibit large jumps within two successive iterations, we choose $\mathbf{x}_p$ equal to the value of $\mathbf{x}$ at the previous iteration, namely, $\mathbf{x}_p = \mathbf{x}_{k-1}$. For this

particular choice of $\mathbf{x}_p$, the standard additive regularization technique can be made equivalent with the multiplicative one, if one chooses the Lagrange multiplier Λ to vary as the iteration proceeds according to

$$\Lambda = \frac{F(\mathbf{x}_k)}{\|\delta\|^2} = \frac{w^e F^e(\mathbf{x}_k)}{\|\delta^e\|^2} + \frac{w^f F^f(\mathbf{x}_k)}{\|\delta^f\|^2}. \tag{22}$$

$F^e(\mathbf{x}_k)$ and $F^f(\mathbf{x}_k)$ denote non-regularized objective functional components for electromagnetic induction and flow (pressure) measurements, respectively. δ^e and δ^f are constants separately determined from the noise level of electromagnetic induction and flow measurements. Similarly, w^e and w^f weight fractions are separately determined for electromagnetic induction and flow measurements. Clearly, $w^e = 1$ and $w^f = 0$ for the single-physics inversion of electromagnetic induction measurements while $w^e = 0$ and $w^f = 1$ for the single-physics inversion of flow measurements. Experience indicates that $w^e = 0.4$ and $w^f = 0.6$ yield results with good accuracy for the joint-inversion problems examined in this paper.

The rationale of multiplicative regularization technique is such that the influence of the regularization factor, Λ, will be high due to the use of a relatively large weighting parameter in the first few iterations of the inversion process, because the value of $F(\mathbf{x}_k)$ is still large. In this case the search direction is predominantly steepest descent, which is a more appropriate approach to use in the initial steps of the inversion process. This is because the optimization using steepest-descent direction has the tendency of suppressing large swings in the search direction. As the iterations proceed, the inversion process will increasingly minimize the data misfit error in the non-regularized objective functional when the regularization factor, $R_k(\mathbf{x})$, approaches a constant value close to one. In this case, the search direction increasingly corresponds to the Gauss-Newton search direction. The Gauss-Newton direction is a more appropriate search direction as the inversion process approaches to the nearest minimum of the objective functional, $F(\mathbf{x})$, where the quadratic model for the objective functional becomes more accurate. For relatively more noise-contaminated measurement data, the non-regularized objective functional, $F(\mathbf{x})$, will approximately remain at a certain value as the inversion process marches closer to the nearest minimum. The presence of the weight introduced by the regularization factor, $R_k(\mathbf{x})$, will be more significant. The proposed regularization method suppresses the measurement-noise in all phases of the inversion process. It also fulfills the need for a larger regularization parameter when the measurements contain significant levels of noise. The inversion process is terminated when either the relative data misfit reaches a prescribed value, the

number of iterations exceeds the prescribed maximum, the differences between two successive iterates of the model parameters or the value of the objective functional is within a prescribed tolerance factor.

4. PHYSICAL CONSTRAINTS FOR INVERSION

To impose *a priori* information, such as positivity or physical maximum and minimum bounds (if available) on the inverted model parameters, we make use of nonlinear transforms such that

$$x_i = f(c_i, x_i^{\min}, x_i^{\max}), \quad -\infty < c_i < \infty, \quad i = 1, 2, \ldots, N, \tag{23}$$

where $x_i^{\max}$ and $x_i^{\min}$ denote the upper and lower physical bounds for the model parameter x_i, respectively. These nonlinear transforms map a constrained minimization problem to an unconstrained one. Above constraints force the model parameters to always remain within their physical bounds.

There exists a number of nonlinear transforms $f(c_i, x_i^{\min}, x_i^{\max})$ that map a constrained minimization problem into an unconstrained one. Among the many we experimented with, the transform that performs best in the examined dual-physics inversion problems is the first transform reported in the Appendix A of [9].

5. COUPLED DUAL-PHYSICS INVERSE PROBLEM

Robust and accurate determination of fluid-flow related petrophysical parameters from borehole measurements is one of the fundamental problems of quantitative well log interpretation. Introduction of the concepts of fluid flow to the analysis of geoelectrical log measurements improves the physical consistency of the interpretation. In addition, log measurements can be jointly inverted with flow measurements (e.g., pressure and pumping rates) to reduce nonuniqueness in the quantitative estimation of petrophysical parameters. We describe below a coupled dual-physics inversion problem employed to evaluate the multiplicative regularization technique. Synthetic measurements are generated by contaminating simulated data (computed via numerical forward models) with various levels of Gaussian random noise.

In the inverse problem, single- or multi-snapshot measurements of the vertical component of the total magnetic field are acquired at multiple receiver locations and frequencies with a depth-profiling induction logging tool [10]. The operating principle of a typical induction logging tool can be summarized as follows: a multi-turn coil supporting a time-varying current generates a magnetic field

that induces electrical currents in subsurface rock formations. An array of receiver coils measures the magnetic field of the source and the secondary currents. Borehole measurements recorded by the receiver coils are processed into depth-dependent functions of apparent conductivity (or resistivity) called the induction log. Typically, multiple induction logs with various depths of penetration (into subsurface rock formations) are generated within one run of the logging tool (in a borehole) since the measurements are acquired for multiple frequencies. We refer to one run of the induction logging tool with "log" in the context of data-acquisition strategies, which will be discussed later in the paper.

We also consider the availability of dual-packer and multiple observation-probe pressure-transient measurements acquired by a wireline formation tester [12]. A wireline formation tester withdraws reservoir fluids from a subsurface rock formation by imposing a prescribed rate schedule. Pressure time-series as a function of fluid withdrawal is recorded at one or more locations in the borehole by gauges that are in direct hydraulic communicaton with formation fluids. Pressure time-series are subsequently inverted to yield hydraulic properties (e.g., permeability) of the tested formation. We will refer to one run of the wireline formation tester tool with "test" in the context of data-acquisition strategies. Time-dependent (transient) wireline formation tester measurements are also simply referred to as pressure measurements.

The forward model for the coupled dual-physics measurements is a nonlinear function of the spatial distribution of permeabilities and porosities and other relevant rock and fluid properties. We assume the availability of other rock and fluid properties from complementary logs and laboratory experiments. The objective is the joint inversion of layer-by-layer horizontal and vertical permeabilities and porosities from single- or dual-snapshot electromagnetic induction and pressure measurements. We only focus on vertical variability in the petrophysical model. Horizontal geological layers of various thicknesses characterize the reservoir geometry. The vector of model parameters, $\mathbf{x}$, is made up of the layer-by-layer parametric spatial distribution of horizontal and vertical permeabilities and porosities. We assume the availability of information about the locations of layer boundaries from other data types such as borehole image logs and core data. Based on the extent of the available measurement data and *a priori* information, an arbitrary combination of the above-mentioned petrophysical parameters can be included in $\mathbf{x}$.

A vertical borehole is considered to intersect a hydrocarbon-bearing horizontal formation composed of three layers. In addition

to the permeable layers, sealing upper and lower shoulder beds are included in the geoelectrical model as shown in Figure 1. From the onset of drilling, the permeable layers are subject to dynamic water-base mud-filtrate invasion. At the first logging time, an array induction log is recorded across the formation. The tool assumed for electromagnetic induction measurements is the Array Induction Imager Tool, AIT$^{\text{TM}}$. This tool is used to ensure the availability of data with multiple depths of penetration [10]. The data-acquisition strategy that employs only the first log is referred to as the log strategy. The second data type is the multi-probe formation pressure measurements acquired with a wireline formation tester tool, namely, Modular Formation Dynamics Tester, MDT$^{\text{TM}}$. A dual-packer/probe configuration with two vertical observation probes is considered as the measurement platform [12]. Given favorable flow conditions and sufficient test duration, pressure measurements conducted by the dual-packer and tandem observation probes contain significant information about horizontal and vertical permeabilities (k_h and k_v) when reliable *a priori* information about the porosity-total compressibility group (ϕC_t) is available. In this work, we assume the availability of laboratory measurements of formation fluid and rock properties that can be incorporated into a subsurface flow simulator. Therefore, in our formulation of the inverse problem, the group described by ϕC_t decouples into two pieces per simulation gridblock: a known C_t and an unknown ϕ which is a model parameter subject to inversion along with k_h and k_v. Additionally, in our forward model, the movement of saturations and salt concentrations due to convective transport of fluids is linked to spatial distributions of conductivity via a saturation equation. Thus, provided that the choice of saturation equation is appropriate for the formation of interest, information about porosity, ϕ, can be robustly estimated from electromagnetic measurements within the framework of joint inversion. For the three-layer formation model, we assume that the layers are isotropic in terms of permeability and enforce $k_h = k_v$ as shown in Figure 1.

Subsequent to the acquisition of the first induction log, the multi-probe formation tester tool is deployed across the formation of interest to conduct pressure measurements. Time-series of pressure responses are recorded at two observation probe locations and at the center of the dual-packer open interval in response to a controlled fluid withdrawal (flow) rate schedule. This measurement strategy involves acquisition of dual-physics data, and is here referred to as the log-test strategy. Alternatively, we investigate the case where an additional post-test electromagnetic induction log senses the perturbed two-phase flow field caused by the formation tester fluid withdrawal. This alternative

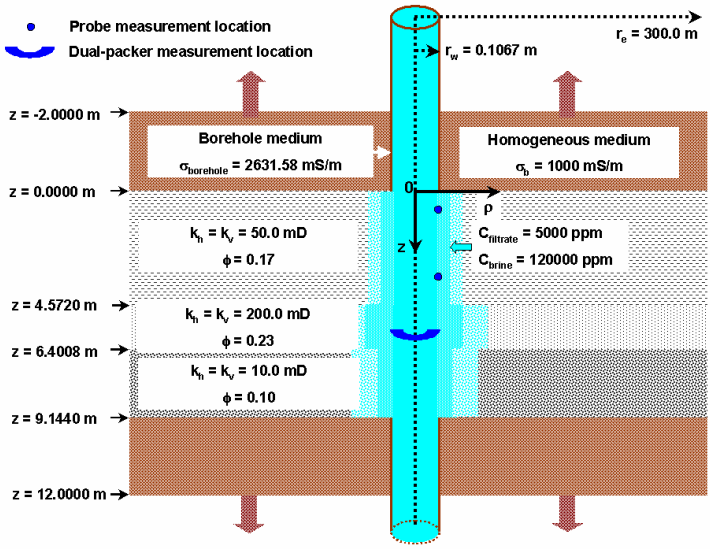

Figure 1. Formation model for the inversion study. Two-dimensional vertical cross-section of the permeable formation intersected by a vertical borehole. The three-layer formation is subject to water-base mud-filtrate invasion.

measurement strategy is here referred to as the log-test-log strategy. In modeling the measurement sequences described above, mud-filtrate invasion is simulated for the entire history of the near-borehole, since the moment of drilling until the acquisition of the last measurement.

On a case-by-case basis, the uncertainty in the inversion outcomes are quantified by computing the Estimator's Covariance Matrix and the Cramer-Rao bounds [2, 9, 15]. In this process, the Estimator's Covariance Matrix is approximated using the (estimated) variance of measurement noise and the inverse of the Gauss-Newton Hessian matrix computed in the final step of the inversion algorithm. The Cramer-Rao error bounds are derived from the information embedded in the diagonal elements of the Estimator's Covariance Matrix. The process of computing the Estimator's Covariance Matrix and the Cramer-Rao bounds is described in detail in [2] and [9]. The uncertainty analysis provides us with error bounds on the inversion results for each inverted parameter. With the purpose of establishing a basis of comparison for the joint-inversion approach that involves the log-test and log-test-log acquisition strategies, we perform single data-type inversions. Inversions of pressure measurements are referred to as the test strategy, and inversions of single- and dual-snapshot

electromagnetic induction logging measurements are respectively referred to as the log and log-log strategies. As in the case of the log-test and log-test-log strategies, the formation is considered to be subject to mud-filtrate invasion during the entire time-interval encompassing each measurement strategy. A quantitative analysis of the uncertainty in the inversion results is carried out via computing the Estimator's Covariance Matrix and the Cramer-Rao bounds as in the case of the joint-inversion approach. For all of the measurement strategies, synthetically generated measurements are contaminated with random Gaussian noise with standard deviation corresponding to 1%, 3%, and 5% of the norm of each individual measurement.

Due to the lack of *a priori* information the weighting matrices of Equation (3), namely, $\mathbf{W}_d$ and $\mathbf{W}_x$, are chosen to be identity matrices. The prior information vector, $\mathbf{x}_p$, in the objective functional of Equation (3) is chosen to be equal to the inverted parameter vector of the previous iteration, namely, $\mathbf{x}_k$. We reduce the possibility of the minimization process to make a large jump from one iteration to another, which improves inversion stability.

The regularization parameter, Λ, is determined via both additive and multiplicative regularization techniques. The number of nonlinear iterations necessary to reduce the value of the objective functional to the level of noise in the measurements is reported for each test problem for the purpose of comparison.

6. COUPLED DUAL-PHYSICS FORWARD MODEL

We use a numerical algorithm designed to simulate the physics of mud-filtrate invasion in vertical and highly deviated boreholes [21]. Numerical modeling of mud-filtrate invasion yields an equivalent time-domain filtrate flow-rate function. Given the pressure overbalance condition, invasion geometry, and mudcake properties, this function models the time-dependent behavior of the mudcake. Due to the fact that clay platelets form a mudcake with permeabilities in the order of 10^{-3} mD, the filtrate invasion rate is predominantly controlled by the mudcake, with minimal influence of the formation permeability [13]. Thus, a numerically computed invasion rate schedule can be imposed as a local source condition to a fluid-flow simulator. As such, the physics of mud-filtrate invasion can be incorporated to a coupled algorithm for the simulation of multi-phase fluid-flow and electromagnetic induction phenomena.

Invasion of water-base mud-filtrate into a partially saturated hydrocarbon-bearing porous medium and a subsequent wireline formation tester fluid withdrawal involve two-phase multi-component

fluid flow. Spatiotemporal distributions of aqueous-phase saturation and salt concentration (in response to the evolution of the pressure field) are modeled as advective transport of hydrocarbon (oleic or gaseous) and aqueous phases, and hydrocarbon (oil or gas), water, and salt components. Ions present in the system are assumed to be soluble only within the aqueous phase and lumped into a single salt component. In the formulation of the forward problem, we assume the existence of a salt concentration contrast between the in-situ formation brine and the invading mud-filtrate. Diffusion has only a small effect at invasion radius length-scales [13]. In addition, the equilibration of salt concentration among pores occurs at time-scales smaller than the invasion time-scale, whereupon local-level aqueous-phase salt concentrations remain the same from pore to pore. Therefore, for the problem of interest, we only consider advective miscible transport of the salt component within the aqueous phase and neglect the diffusional spreading of the interface between mud-filtrate and formation brine.

Simulation of isothermal two-phase flow in a partially saturated hydrocarbon-bearing medium requires mass balance and transport equations as well as a constitutive equation of state. We disregard the presence of chemical reactions, rock/fluid mass transfer, and diffusive/dispersive transport. The mass balance equation for the ith fluid phase can be stated as follows [5]

$$\frac{\partial(\rho_i \phi S_i)}{\partial t} + \nabla \cdot (\rho_i \upsilon_i) = -q_{vi}, \quad i = 1, 2. \tag{24}$$

For the two-phase immiscible flow of aqueous (components: water and salt) and oleic (component: liquid hydrocarbon (oil)) phases as in the problems considered in this paper, $i = 1$ denotes the aqueous phase and $i = 2$ denotes the oleic phase. We model flow in the near-borehole region of a single vertical well intersecting a hydrocarbon-bearing horizontal reservoir in R^3. The cylindrical coordinate system is employed to accurately model the flows associated with mud-filtrate invasion and wireline formation tester fluid withdrawal. Spatial support for material balance equations is then $\Omega = \{(r, \theta, z) \in R^3 : r_w \leq r \leq r_e, 0 \leq \theta \leq 2\pi, 0 \leq z \leq h\}$. In Equation (24), ρ, υ, ϕ, q_v, and S denote fluid density, fluid velocity vector, porosity, source/sink term (accounting for the fluid mass supplied/extracted from the pore-space via injection/production probes or wells), and fluid-phase saturation, respectively. The subscript i designates the fluid-phase index. Moreover, r_w, r_e, and h stand for borehole radius, external radius of the formation, and total formation thickness, respectively. No-flow boundary conditions are imposed on the upper, lower, and outer limits of the formation. The external boundary of the formation

is located relatively far away from the wellbore. A constant rate internal boundary condition is imposed to the borehole wall time-step-by-time-step. Time-variant invasion rate history and other formation test related rate schedules are incorporated into our simulations in a time-stepwise discrete fashion. In our formulation, Darcy's law is the governing transport equation, i.e.,

$$v_i = -\overline{\overline{\mathbf{k}}} \cdot \frac{k_{ri}}{\mu_i}(\nabla p_i - \rho_i g \nabla D_z), \quad i = 1, 2. \tag{25}$$

In Equation (25), $\overline{\overline{\mathbf{k}}}$ is the absolute permeability tensor of the porous medium, k_r is the fluid-phase relative permeability, μ is the fluid-phase viscosity, p is the fluid-phase pressure, ρ is the fluid-phase density, g is the gravitational acceleration, and D_z is the vertical location below some reference level. Finally, the constituent equation follows from the equation of state. The assumption is also made that both fluid-phase and rock compressibilities are constant, and are given by

$$c_{fluid,i} = \frac{1}{\rho_i} \left. \frac{\partial \rho_i}{\partial p_i} \right|_T, \quad i = 1, 2 \tag{26}$$

and

$$c_{rock} = \frac{1}{\phi} \left. \frac{\partial \phi}{\partial p_{avg.}} \right|_T, \tag{27}$$

respectively. In Equation (27), $p_{avg.}$ stands for the average fluid pressure. The above assumption of constant fluid compressibility does not hold for the two-phase flow of gaseous and aqueous phases. Thus, for such cases, gas compressibility is treated as a function of the PVT properties of gas for each time-step. Capillary pressures and fluid saturations are governed by

$$P_c = p_{nw} - p_w, \tag{28}$$

and

$$S_{nw} + S_w = 1.0, \tag{29}$$

where the subscripts nw and w stand for nonwetting phase and wetting phase, respectively. Typically, oleic phase is the nonwetting phase and aqueous phase is the wetting phase for two-phase immiscible flow problems in sandstone formations like the ones considered in this paper.

Advective transport of the salt component is simulated after a converged solution for the time-step has been found, and the interblock flows are determined. A mass conservation equation is solved to update the spatial distribution of salt concentrations, C_w, and is given by

$$\frac{\partial(\rho_w \phi S_w C_w)}{\partial t} + \nabla \cdot (\rho_w v_w C_w) = -C_{wi} q_i. \tag{30}$$

In Equation (30), C_{wi} and q_i stand for the concentration of invading mud-filtrate, and invasion rate at a given time-step, respectively. Numerical solution of the two-phase, three-component fluid-flow problem is carried out using a commercial reservoir simulator on a 3D cylindrical mesh.

Spatial distributions of aqueous-phase saturation corresponding to each logging time are subsequently transformed into snapshots of electrical conductivity using Archie's law,

$$\sigma = (1/a)\sigma_w \phi^m S_w^n, \tag{31}$$

[4] applied gridblock-by-gridblock. In the above equation, σ, σ_w, and S_w denote formation conductivity, brine conductivity, and aqueous-phase saturation, respectively. Porosity and saturation exponents m and n, and the normalization parameter a are empirical constants documented in Table 1. Characteristic values for sandstone reservoirs are selected for the studies reported in this paper.

Spatial distributions of brine conductivity at each logging time are computed from (simulated) salt concentrations using the following equation [23]

$$\sigma_w = \left[\left(0.0123 + \frac{3647.5}{C_w^{0.955}}\right)\frac{82}{1.8T + 39}\right]^{-1}, \tag{32}$$

where C_w and T stand for salt concentration in [ppm] and formation temperature in [°C], respectively. As such, the dependency of conductivity on the aqueous-phase salt concentration is taken into account. The main assumption underlying the brine conductivity model is the instantaneous temperature equilibrium between invading and in-situ aqueous phases.

Forward modeling of array induction logging tool responses requires the solution of a frequency-domain electromagnetic induction problem described by the Maxwell's equations formulated for a diffusive electromagnetic field. The basic equations governing the local behavior of the diffusive electromagnetic field, assuming a time-harmonic variation of the form $e^{i\omega t}$, where $i^2 = -1$, ω is angular frequency, and t is time, present in an inhomogeneous, isotropic, and nonmagnetic medium, can be stated as follows:

$$\nabla \times \mathbf{E} + i\omega\mu\mathbf{H} = 0, \tag{33a}$$

$$\nabla \times \mathbf{H} - \sigma\mathbf{E} = \mathbf{J}. \tag{33b}$$

Here, $\mathbf{E}$ is the electric field vector, $\mathbf{H}$ is the magnetic field vector, and $\mathbf{J}$ is the external electric current source vector. The symbols $\sigma = \sigma(x, y, z)$ and μ denote the conductivity coefficient and the magnetic permeability, respectively. Consistent with the nature of low-frequency electromagnetic induction applications, the displacement

Table 1. Summary of geometrical, petrophysical, mudcake, fluid, and sensor parameters for the formation model.

Variable	Unit	Value
Mudcake permeability	[mD]	0.010
Mudcake porosity	[fraction]	0.400
Mud solid fraction	[fraction]	0.500
Mudcake maximum thickness	[cm]	1.270
Formation rock compressibility	[kPa^{-1}]	7.252×10^{-10}
Aqueous-phase viscosity (mud-filtrate)	[Pa.s]	1.274×10^{-3}
Aqueous-phase density (mud-filtrate)	[g/cm^3]	1.001
Aqueous-phase formation volume factor (mud-filtrate)	[res. m^3/std. m^3]	0.996
Aqueous-phase compressibility (mud-filtrate)	[kPa^{-1}]	3.698×10^{-7}
Oleic-phase viscosity	[Pa.s]	3.550×10^{-4}
Oleic-phase API density	[°API]	42
Oleic-phase density	[g/cm^3]	0.816
Oleic-phase formation volume factor	[res. m^3/std. m^3]	1.471
Oleic-phase compressibility	[kPa^{-1}]	2.762×10^{-6}
Viscosity ratio (water-to-oil)	[dimensionless]	3.589
Formation pressure at the formation top (at the reference depth = 0 m)	[MPa]	20.684
Mud hydrostatic pressure	[MPa]	24.821
Wellbore radius	[m]	0.108
Formation outer boundary location	[m]	300.000
Formation temperature	[°C]	104.444
a-constant in the Archie's equation	[dimensionless]	1.000
m-cementation exponent in the Archie's equation	[dimensionless]	2.000
n-water saturation exponent in the Archie's equation	[dimensionless]	2.000
Mud conductivity	[mS/m]	2631.579
Upper and lower shoulder bed conductivities	[mS/m]	1000.000
Logging interval	[m]	6.096×10^{-1}
Specific Information for the Wireline Formation Test:		
Drawdown duration	[min.]	100.000
Build-up duration	[min.]	100.000
Drawdown rate	[m^3/d]	3.339
Interval sealed by the dual-packer (DP) module (wrt. to the formation top)	[m]	5 639 to 6.553
Location of the first observation probe (wrt. to the formation top)	[m]	1.524
Location of the second observation probe (wrt. to the formation top)	[m]	3.962
Location of the pressure measurement conducted by DP module (wrt. to the formation top)	[m]	6.096

current is assumed to be negligible. Equations (33a) and (33b) can be combined into the following equation for electric field $\mathbf{E}$,

$$\sigma^{-1}\nabla \times \nabla \times \mathbf{E} + i\,\omega\,\mu\mathbf{E} = -i\omega\,\mu\,\sigma^{-1}\mathbf{J}. \tag{34}$$

A finite-difference stencil is employed on a set of staggered grid for the numerical solution of Equation (34) to yield multi-frequency simulations of induction logging tool responses [6]. Spatial distributions of conductivity, σ, are computed from flow simulation results, namely, aqueous-phase saturations and salt concentrations at each logging time. Conductivities computed from flow simulations on the 3D cylindrical grid are mapped to the 3D Cartesian grid by means of a homogeneization stencil [11]. Induction logging tool responses are simulated for each conductivity snapshot in time.

As shown in Equations (24) through (30), there exists a nonlinear coupling between fluid-phase pressure (p), water saturation (S_w), and

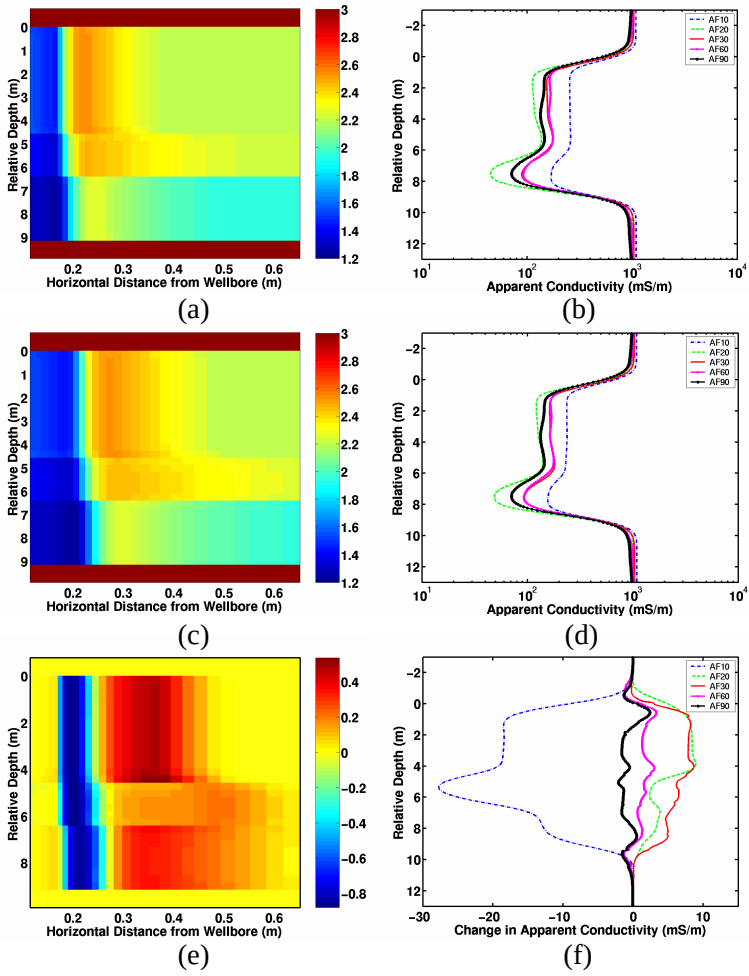

Figure 2. Log-log measurement strategy: (a) Conductivity domain represented in logarithmic scale $[\log_{10}(\sigma)]$ at $t_{\log 1} = 1.5\,\text{day}$, and (b) the corresponding electromagnetic induction logging measurements (AF10 through AF90 indicate measurements with various depths of penetration, AF10 corresponding to the shallowest and AF90 corresponding to the deepest measurement). (c) Conductivity domain in logarithmic scale $[\log_{10}(\sigma)]$ at $t_{\log 2} = 3.0\,\text{day}$, and (d) the corresponding electromagnetic induction logging measurements. (e) Normalized variation in the conductivity domain $[\sigma_2(\mathbf{r}) - \sigma_1(\mathbf{r})]/\sigma_1(\mathbf{r})$, and (f) the change in the induction log response from $t_{\log 1}$ to $t_{\log 2}$, namely, $[\sigma_{app.t2} - \sigma_{app.t1}]$.

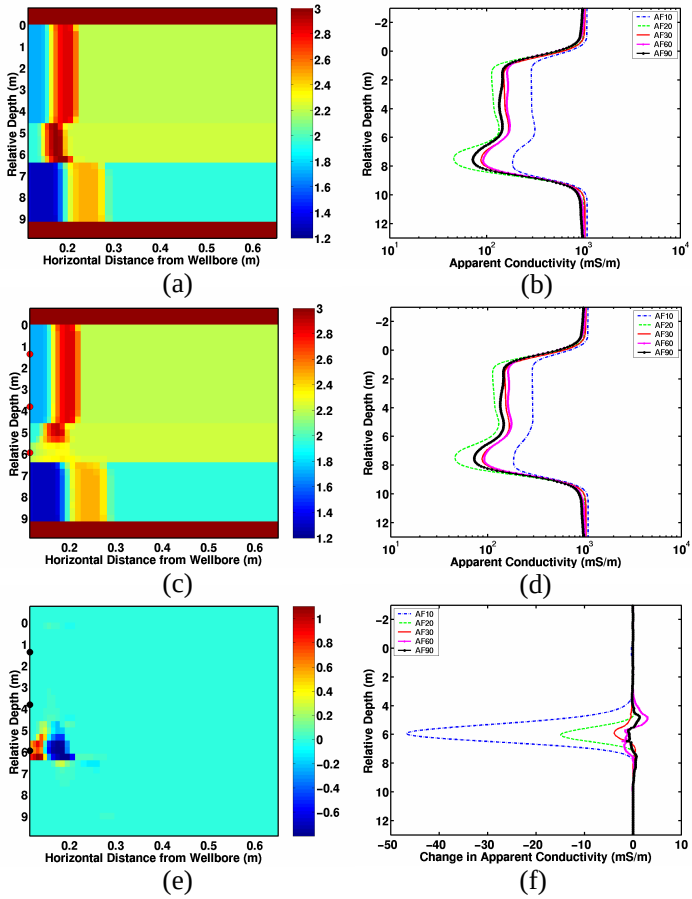

Figure 3. Log-test-log measurement strategy: (a) Conductivity domain represented in logarithmic scale $[\log_{10}(\sigma)]$ at $t_{\log 1} = 1.5$ day, and (b) the corresponding electromagnetic induction logging measurements (AF10 through AF90 indicate measurements with various depths of penetration, AF10 corresponding to the shallowest and AF90 corresponding to the deepest measurement). (c) Conductivity domain in logarithmic scale $[\log_{10}(\sigma)]$ at $t_{\log 2} = 1.64$ day (right after the wireline formation test), and (d) the corresponding electromagnetic induction logging measurements. (e) Normalized variation in the conductivity domain $[\sigma_2(\mathbf{r}) - \sigma_1(\mathbf{r})]/\sigma_1(\mathbf{r})$, and (f) the change in the induction log response from $t_{\log 1}$ to $t_{\log 2}$, namely, $[\sigma_{app.t2} - \sigma_{app.t1}]$. Formation tester measurement locations are shown using small circles on the conductivity domain plots corresponding to $t_{\log 2}$.

salt concentration (C_w) variables. These variables are jointly solved by a numerical simulation algorithm on a finite-difference grid. The coupling between multi-phase fluid-flow and electromagnetic induction physics can be explained in simple terms as follows: A change in the pressure field (for example, due to mud-filtrate invasion, fluid withdrawal during a wireline formation test, etc.) results in a potential difference that gives rise to a velocity field and streamlines along which saturation and concentration fronts travel. The coupling between multi-phase fluid-flow and electromagnetic induction physics occurs through S_w and C_w variables as shown in Equation (31) (Archie's law) and Equation (32). These equations give rise to a time-dependent spatial distribution of conductivity (σ). σ-fields corresponding to log-acquisition times are fed to a finite-difference-based algorithm that models induction tool responses. Example evolutions of conductivity fields as a function of mud-filtrate invasion and wireline formation testing related fluid-flow phenomena are shown in Figures 2 and 3, respectively. Simulated log responses (corresponding to illustrated conductivity field snapshots) and time-lapse induction logging signals are also shown in these figures. Time-lapse signals clearly demonstrate the sensitivity of log responses to near-borehole fluid-flow phenomena governed by such formation properties as permeability and porosity.

7. NUMERICAL EXAMPLES

7.1. Isotropic Permeability Model

Mudcake characteristics, formation rock and fluid properties, and specific instrumental/acquisition details are listed in Table 1. We use a $121 \times 1 \times 30$ ($r \times \theta \times z$) grid in the cylindrical coordinate system as the result of extensive finite-difference gridding studies to produce computationally efficient, internally consistent, and accurate numerical simulations. The grid is uniform in the vertical direction. Block sizes increase logarithmically in the radial direction away from the borehole. We also use a relatively fine cylindrical finite-difference grid of size $141 \times 1 \times 30$ in the fluid-flow simulations performed for generating the synthetic measurements. Simulations carried out using fine and coarse grids agree within 1% of each other. Layer-by-layer relative permeability and capillary pressure functions are reported in [2] together with the remaining details of the forward model. An averaged mud-filtrate invasion rate history is imposed on the fluid-flow simulator as the source condition. For the log-log strategy, the invasion rate history is extended further until the second logging time [3rd day]. The rate-domain response of the mudcake removal (due to drill-string trip-out at the first logging time [1.5th day]) is also incorporated to

the mud-filtrate invasion history.

The following schedule is assumed for the log-test strategy. The induction log is recorded at the 1.5th day of mud-filtrate invasion. A subsequent wireline formation test is scheduled to last 200 minutes. During the formation test, fluid is withdrawn from the formation at a constant liquid rate of 3.34 m^3/d for 100 minutes and the formation pressure drawdown response is observed across the dual-packer interval and at the observation probes. Subsequently, the tool is shut-down for another 100 minutes and the formation pressure build-up response is recorded. Upon conclusion of the formation test, a second induction log is recorded in the log-test-log data-acquisition schedule.

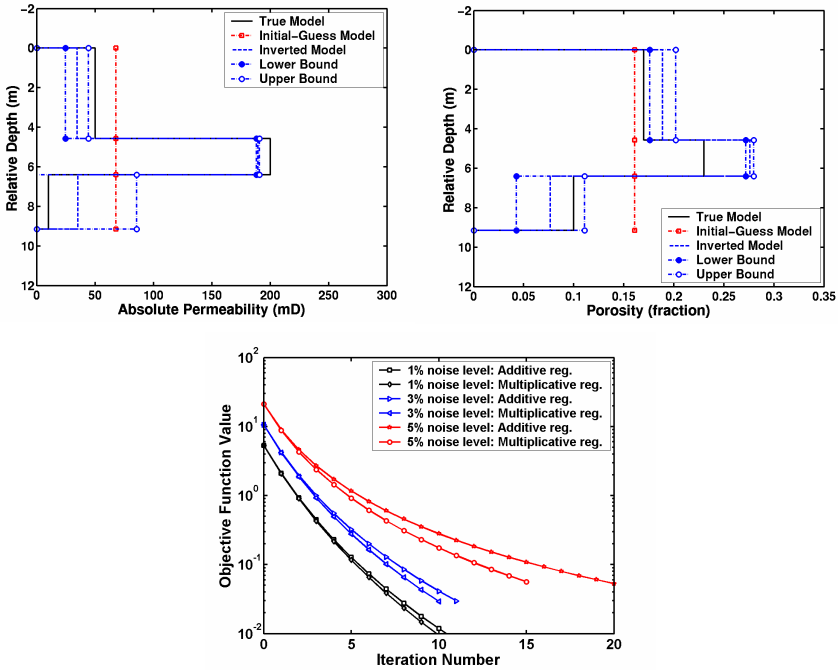

Figure 4. Top panels: Permeability and porosity profiles yielded by the multiplicative regularized inversion of pressure-transient measurements (acquired by the wireline formation tester probes subsequent to a 1.5 day-long mud-filtrate invasion) [test strategy]. Measurements are contaminated with 3% Gaussian, random noise. The Cramer-Rao bounds (with 99.7% probability) for the inversion results are computed post-convergence. The initial-guess model parameter values are also shown. The bottom panel shows the misfit reduction plot for all investigated noise-contamination levels (1%, 3%, and 5%).

The induction log is recorded at the 1.5th day of invasion in the single-snapshot strategy. In the dual-snapshot log strategy, an additional induction log is acquired at the 3rd day of invasion to track the changes in the near-borehole saturation and salt concentration distributions due to mud-filtrate invasion. Transient wireline formation tester measurements simulated for the test-log strategy are used for the independent inversion of pressure measurements (test strategy). Two-phase displacement, production, and shut-in periods associated with the mud-filtrate invasion, the formation-test drawdown, and the formation-test build-up processes are forward modeled within the context of iterative inversion.

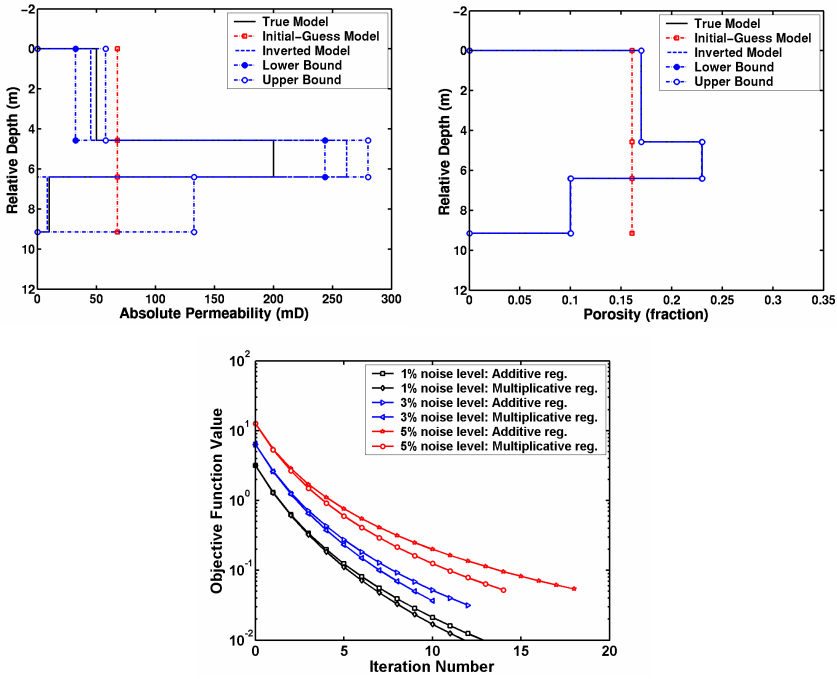

Figure 5. Top panels: Permeability and porosity profiles yielded by the multiplicative regularized inversion of single-time induction logging measurements (acquired by the AIT tool subsequent to a 1.5 day-long mud-filtrate invasion) [log strategy]. Measurements are contaminated with 3% Gaussian, random noise. The Cramer-Rao bounds (with 99.7% probability) for the inversion results are computed post-convergence. The initial-guess model parameter values are also shown. The bottom panel shows the misfit reduction plot for all investigated noise-contamination levels (1%, 3%, and 5%).

Permeability and porosity profiles yielded by the (independent) inversion of pressure measurements (test strategy) are shown in the top panels of Figure 4 for a noise-contamination level of 3%. Inversion results are only shown for the multiplicative regularization approach as they are almost identical to the ones obtained via additive regularization. True and initial-guess profiles for the model parameters (subject to inversion) are also shown in the panels of this figure to quantify the accuracy and robustness of the inversion results. On the other hand, the degrees of uncertainty associated with the inversion

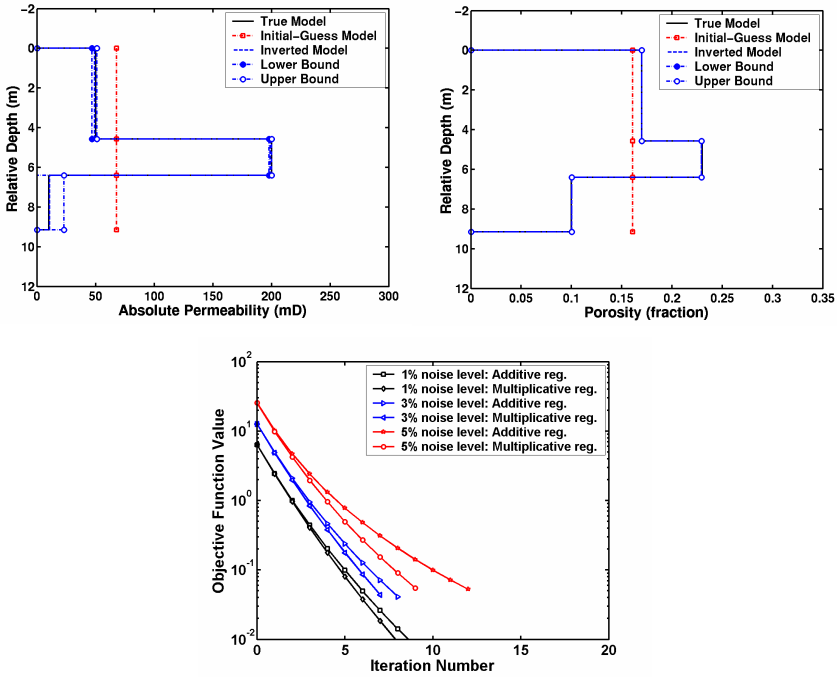

Figure 6. Top panels: Permeability and porosity profiles yielded by the multiplicative regularized joint inversion of single-time induction logging measurements (acquired by the AIT tool) and pressure-transient measurements (acquired by the wireline formation tester probes subsequent to a 1.5 day-long mud-filtrate invasion) [log-test strategy]. Measurements are contaminated with 3% Gaussian, random noise. The Cramer-Rao bounds (with 99.7% probability) for the inversion results are computed post-convergence. The initial-guess model parameter values are also shown. The bottom panel shows the misfit reduction plot for all investigated noise-contamination levels (1%, 3%, and 5%).

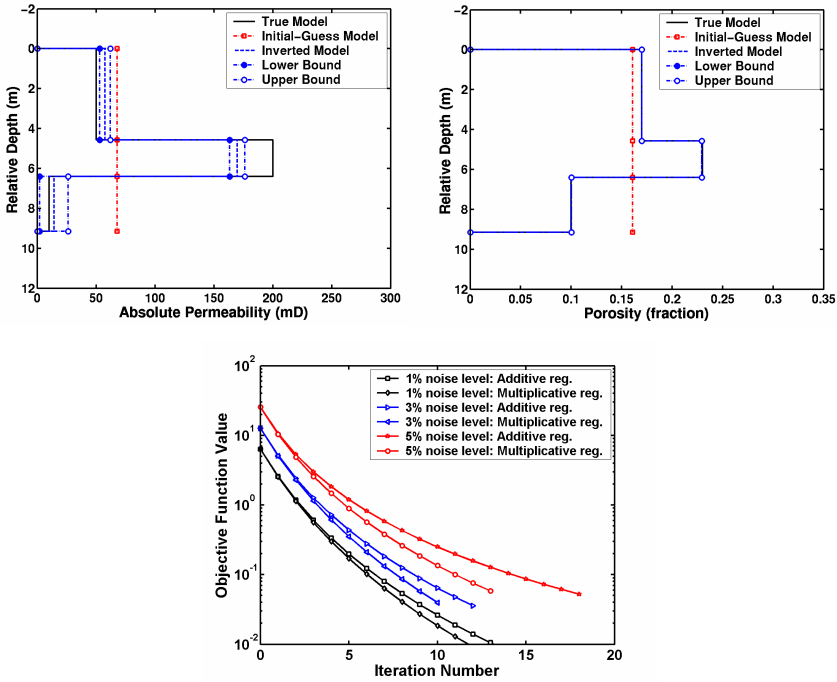

Figure 7. Top panels: Permeability and porosity profiles yielded by the multiplicative regularized joint inversion of two-snapshot induction logging measurements (acquired by the AIT tool) [log-log strategy]. The first induction log was acquired subsequent to a 1.5 day-long mud-filtrate invasion. A second induction log was acquired at the 3rd day of mud-filtrate invasion. Measurements are contaminated with 3% Gaussian, random noise. The Cramer-Rao bounds (with 99.7% probability) for the inversion results are computed post-convergence. The initial-guess model parameter values are also shown. The bottom panel shows the misfit reduction plot for all investigated noise-contamination levels (1%, 3%, and 5%).

results are quantified by computing the Estimator's Covariance Matrix and the 99.7% probability-level Cramer-Rao bounds [2, 9]. These bounds provide error bars for the inverted model parameters. The progress of the misfit reduction as a function of nonlinear inversion iterations is shown in the bottom panel of Figure 4 for both additive and multiplicative regularization techniques and for all investigated noise-contamination levels (1%, 3%, and 5% Gaussian random noise). Inversion results and post-inversion uncertainty analyses are shown for the log strategy in Figure 5, for the log-test strategy in Figure 6, for

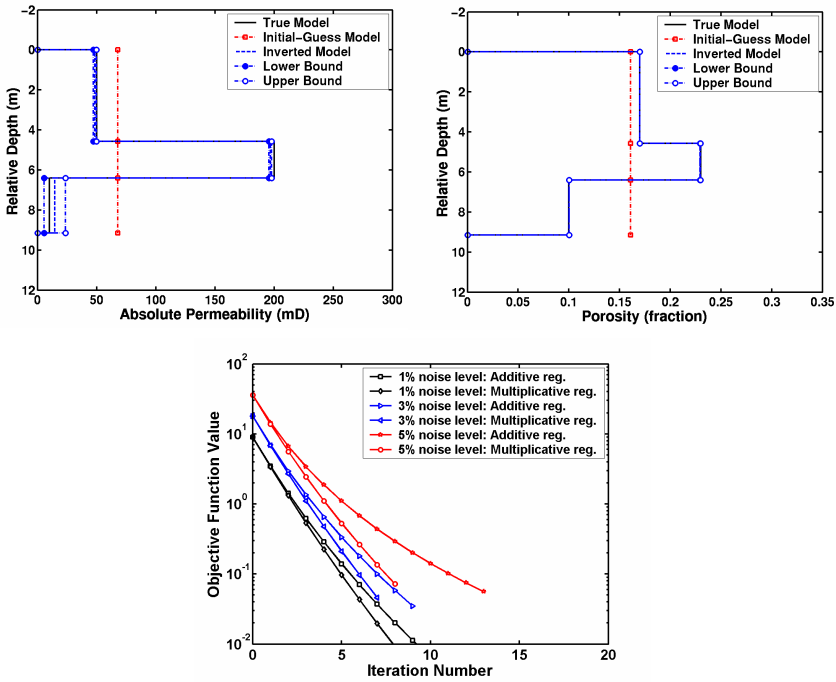

Figure 8. Top panels: Permeability and porosity profiles yielded by the joint inversion of two-snapshot induction logging measurements (acquired by the AIT tool) and pressure-transient measurements (acquired by the wireline formation tester probes) [log-test-log strategy]. The first induction log and the formation test were conducted subsequent to a 1.5 day-long mud-filtrate invasion. A second induction log was acquired right after the formation test. Measurements are contaminated with 3% Gaussian, random noise. The Cramer-Rao bounds (with 99.7% probability) for the inversion results are computed post-convergence. The initial-guess model parameter values are also shown. The bottom panel shows the misfit reduction plot for all investigated noise-contamination levels (1%, 3%, and 5%).

the log-log strategy in Figure 7, and for the log-test-log strategy in Figure 8.

Inversion results indicate that the simultaneous use of coupled dual-physics data sets effectively reduces the nonuniqueness, improves the stability of the minimization scheme, and yields more accurate inversions. Although the inverted permeability and porosity profiles are not shown for all investigated noise-contamination levels, it was observed that the constructive impact of dual-physics data sets

becomes increasingly significant when the measurements contain high levels of noise. The inversion results remain robust for all noise levels with the multiplicative regularization approach. A similar trend is also observed for the additive regularization approach: the inverted model parameters are of acceptable accuracy. Having stated that, in relative terms, the accuracies of the inverted model parameters are typically lower with the additive regularization approach for the 5% noise level. Misfit reduction profiles signify that the multiplicative regularization method consistently yields more rapid convergence compared to the additive regularization method.

7.2. Transversely Anisotropic Permeability Model

A three-layer formation exhibiting permeability anisotropy is considered for inversion. Synthetic single-time electromagnetic induction logging and wireline formation tester pressure measurements (subsequent to a 1.5 day-long mud-filtrate invasion) are generated for the formation model shown in Figure 9 using the same reservoir fluid properties and measurement strategies described for the isotropic case. Formation layers are assumed to be in hydraulic communication. Horizontal permeability, vertical permeability, and porosity profiles yielded by joint inversions of pressure and electromagnetic measurements (log-test

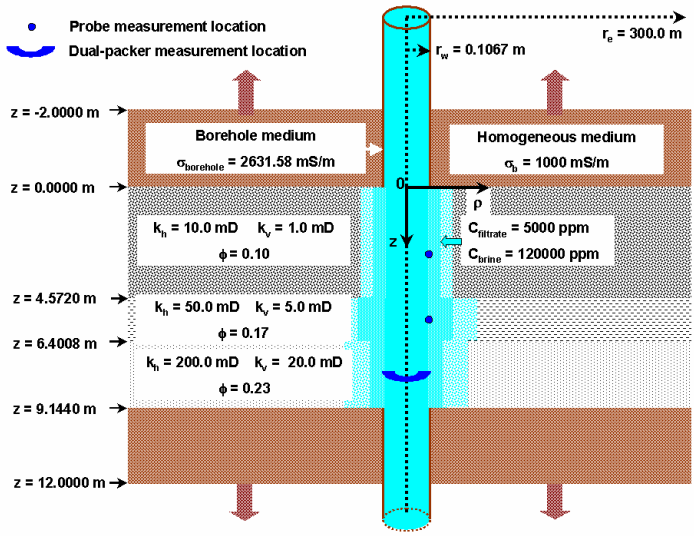

Figure 9. Two-dimensional vertical cross-section of the anisotropic formation intersected by a vertical borehole. The three-layer formation is subject to water-base mud-filtrate invasion.

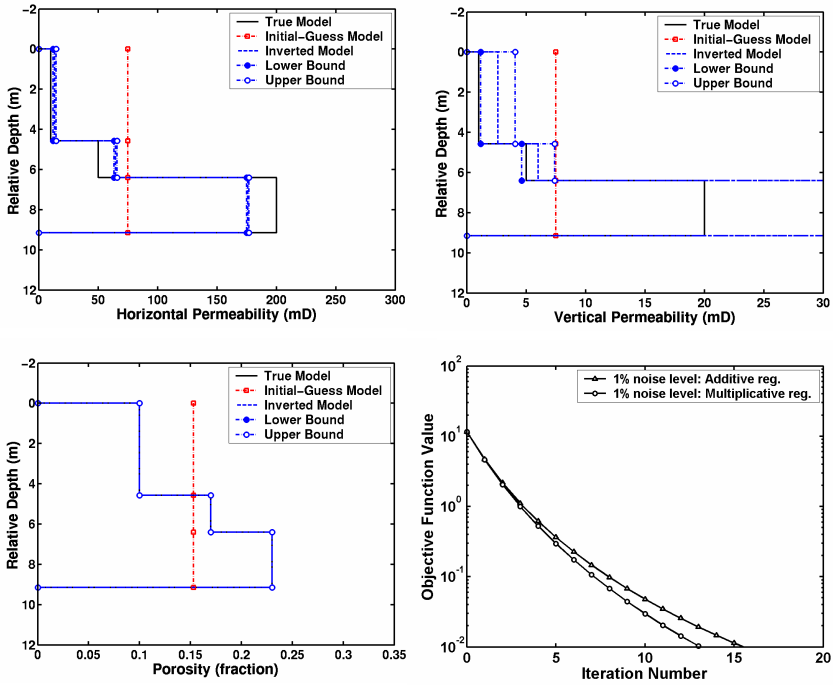

Figure 10. Horizontal permeability, vertical permeability, and porosity profiles yielded by the multiplicative regularized joint inversion of single-time induction logging measurements (acquired by the AIT tool) and pressure-transient measurements (acquired by the wireline formation tester probes subsequent to a 1.5 day-long mud-filtrate invasion) [log-test strategy]. The Cramer-Rao bounds (with 99.7% probability) for the inversion results are computed post-convergence. Inversion results are shown for the cases where measurements are contaminated with 1% Gaussian, random noise. The initial-guess model parameter values are also shown. The last panel shows the misfit reduction plot.

strategy) are shown in the panels of Figure 10 for 1%, Figure 11 for 3%, and Figure 12 for 5% noise level. Inversion results are only shown for the multiplicative regularization approach as they are almost identical to that obtained via additive regularization.

Inverted values of horizontal permeability and porosity remain fairly consistent with the true profiles. Although estimations exhibit inaccuracies for 1% and 3% noise levels, the trends of inverted vertical permeability values for the first and second layers (from the top of the

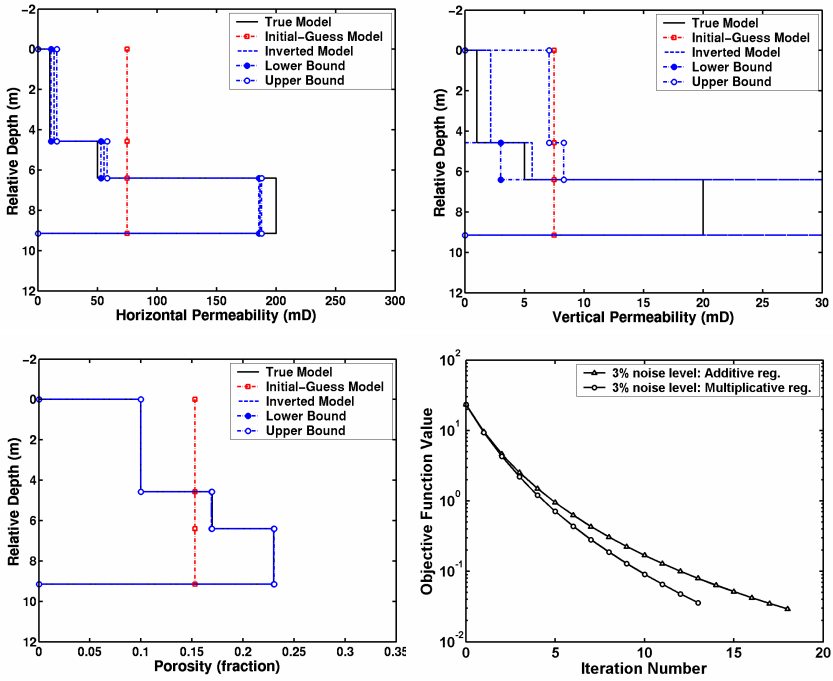

Figure 11. Horizontal permeability, vertical permeability, and porosity profiles yielded by the multiplicative regularized joint inversion of single-time induction logging measurements (acquired by the AIT tool) and pressure-transient measurements (acquired by the wireline formation tester probes subsequent to a 1.5 day-long mud-filtrate invasion) [log-test strategy]. The Cramer-Rao bounds (with 99.7% probability) for the inversion results are computed post-convergence. Inversion results are shown for the cases where measurements are contaminated with 3% Gaussian, random noise. The initial-guess model parameter values are also shown. The last panel shows the misfit reduction plot.

formation) remain consistent with the true trend. For the 5% noise level, the estimation error increases for the vertical permeability of these layers. The inverted vertical permeability value for the bottom-most (third) layer diverges from the true value for all noise levels. It exceeds the plotting scale in Figure 10 and Figure 11.

While the estimations of horizontal permeability and porosity profiles remain accurate and error bounds are sufficiently narrow for all investigated noise levels, the estimations of the vertical permeability

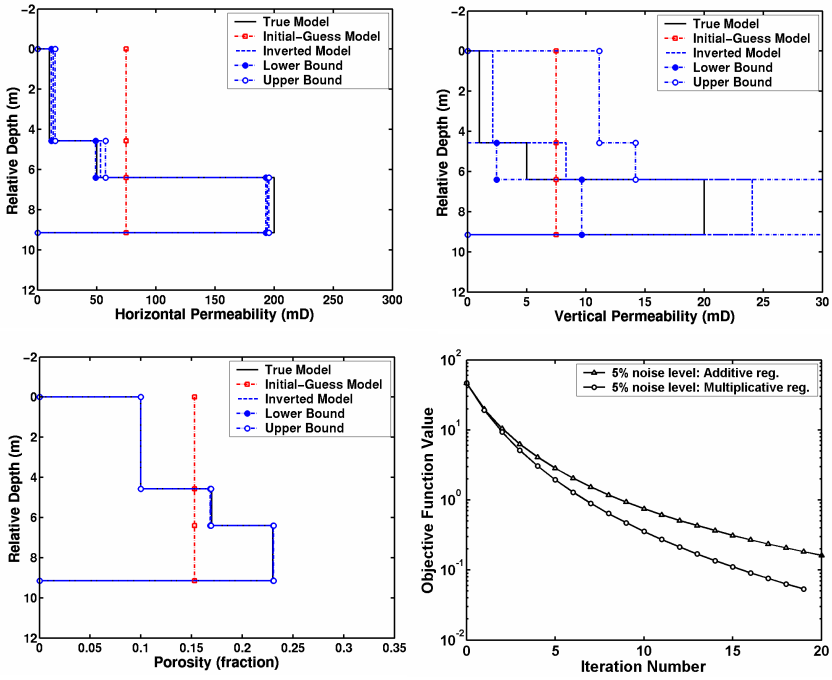

Figure 12. Horizontal permeability, vertical permeability, and porosity profiles yielded by the multiplicative regularized joint inversion of single-time induction logging measurements (acquired by the AIT tool) and pressure-transient measurements (acquired by the wireline formation tester probes subsequent to a 1.5 day-long mud-filtrate invasion) [log-test strategy]. The Cramer-Rao bounds (with 99.7% probability) for the inversion results are computed post-convergence. Inversion results are shown for the cases where measurements are contaminated with 5% Gaussian, random noise. The initial-guess model parameter values are also shown. The last panel shows the misfit reduction plot.

profile exhibit significant inaccuracies. The error bounds are relatively larger for the inverted vertical permeabilities in comparison to other model parameters. In the test problem, there are very few pressure sensors (or measurement locations) across the three-layer formation to provide sufficiently informative pressure information under layer-to-layer crossflow conditions. Therefore, the inversion algorithm cannot extract the vertical permeability values correctly from noise-contaminated measurements. Although the multiplicative

regularization method delivers more rapid convergence compared to the additive regularization method for the anisotropic inversion problem, it falls short in increasing the accuracy of the inversion results.

8. SUMMARY AND CONCLUSIONS

The formulation of the multiplicative regularization technique, originally developed for the conjugate gradient type imaging algorithms, is extended and successfully applied to a weighted and regularized Gauss-Newton parametric joint-inversion algorithm. The algorithm is employed for the quantitative joint and independent inversions of electromagnetic induction logging and formation tester transient pressure measurements. The benefit of the inversion algorithm is the quantitative estimation of layer-by-layer permeabilities and porosities. The multiplicative regularization method delivers better convergence rates compared to the additive regularization method for all investigated problems. The convergence performance of the multiplicative regularization method is significantly better than the additive regularization method as a function of increasing levels of measurement noise.

Inversion results indicate that the simultaneous use of coupled dual-physics data sets effectively reduces the nonuniqueness and improves the stability of the minimization scheme. The positive impact of dual-physics data sets becomes significant when the measurements contain high levels of noise.

REFERENCES

1. Abubakar, A., P. M. van den Berg, and S. Y. Semenov, "Two- and three-dimensional algorithms for microwave imaging and inverse scattering," *Journal of Electromagnetic Waves and Applications*, Vol. 17, No. 2, 209–231, 2003.
2. Alpak, F. O., "Algorithms for numerical modeling and inversion of multi-phase fluid-flow and electromagnetic measurements," Ph.D. Dissertation, Department of Petroleum and Geosystems Engineering, The University of Texas at Austin, 2005.
3. Alpak, F. O., T. M. Habashy, C. Torres-Verdín, and E. B. Dussan V., "Joint inversion of transient-pressure and time-lapse electromagnetic logging measurements," *Petrophysics*, Vol. 45, No. 3, 251–267, 2004.
4. Archie, G. E., "The electrical resistivity log as an aid

in determining some reservoir characteristics," *Trans. AIME*, Vol. 146, 54–62, 1942.

5. Aziz, K. and A. Settari, *Petroleum Reservoir Simulation*, Applied Science Publishers, London, 1979.
6. Druskin, V., L. Knizhnerman, and P. Lee, "New spectral Lanczos decomposition method for induction modeling in arbitrary 3D geometry," *Geophysics*, Vol. 64, 701–706, 1999.
7. Epov, M., I. Yeltsov, A. Kashevarov, A. Sobolev, and V. Ulyanov, "Time evolution of the near borehole zone in sandstone reservoir through the time-lapse data of high-frequency electromagnetic logging," *Proceedings of the 43rd Annual Logging Symposium: Society of Well Log Analysts*, Paper ZZ, 1–10, Oiso, Japan, Jun. 2–5, 2002.
8. Gill, P. E., W. Murray, and M. H. Wright, *Practical Optimization*, Academic Press, London, 1981.
9. Habashy, T. M. and A. Abubakar, "A general framework for constraint minimization for the inversion of electromagnetic measurements," *Progress In Electromagnetics Research*, Vol. 46, 265–312, 2004.
10. Hunka, J. F., T. D. Barber, R. A. Rosthal, G. N. Minerbo, E. A. Head, A. Q. Howard, G. A. Hazen, and R. N. Chandler, "A new resistivity measurement system for deep formation imaging and high-resolution formation evaluation," *Proceedings of the Annual Technical Conference and Exhibition: Society of Petroleum Engineers*, Paper SPE 20559, 295–307, New Orleans, Lousiana, Sep. 23–26, 1990.
11. Moskow, S., V. Druskin, T. Habashy, P. Lee, and S. Davydycheva, "A finite difference scheme for elliptic equations with rough coefficients using a Cartesian grid nonconforming to interfaces," *SIAM Journal on Numerical Analysis*, Vol. 36, No. 2, 442–464, 1999.
12. Pop, J., R. Badry, C. Morris, D. Wilkinson, P. Tottrup, and J. Jonas, "Vertical interference testing with a wireline-conveyed straddle-packer tool," *Transactions of the Annual Technical Conference and Exhibition: Society of Petroleum Engineers*, Paper SPE 26481, 665–680, Houston, Texas, Oct. 3–6, 1993.
13. Ramakrishnan, T. S. and D. J. Wilkinson, "Formation producibility and fractional flow curves from radial resistivity variation caused by drilling fluid invasion," *Physics of Fluids*, Vol. 9, No. 4, 833–844, 1997.
14. Ramakrishnan, T. S. and D. J. Wilkinson, "Water-cut and fractional flow logs from array-induction measurements," *SPE*

Reservoir Evaluation and Engineering, Vol. 2, No. 1, 85–94, 1999.

15. Scharf, L. L., *Statistical Signal Processing, Detection, Estimation, and Time Series Analysis*, Addison-Wesley, Massachusetts, 1991.
16. Semmelbeck, M. E., J. T. Dewan, and S. A. Holditch, "Invasion-based method for estimating permeability from logs," *Proceedings of the Annual Technical Conference and Exhibition: Society of Petroleum Engineers*, Paper SPE 30581, 517–531, Dallas, Texas, Oct. 22–25, 1995.
17. Tobola, D. P. and S. A. Holditch, "Determination of reservoir permeability from repeated induction logging," *SPE Formation Evaluation*, 20–26, Mar. 1991.
18. Van Den Berg, P. M. and A. Abubakar, "Contrast source inversion method: State of art," *Progress In Electromagnetics Research*, Vol. 34, 189–218, 2001.
19. Van Den Berg, P. M., A. Abubakar, and J. T. Fokkema, "Multiplicative regularization for contrast profile inversion," *Radio Science*, Vol. 38, No. 2, 23.1–23.10, 2003.
20. Yao, C. Y. and S. A. Holditch, "Reservoir permeability estimation from time-lapse log data," *SPE Formation Evaluation*, 69–74, Jun. 1996.
21. Wu, J., C. Torres-Verdín, M. A. Proett, K. Sepehrnoori, and D. Belanger, "Inversion of multi-phase petrophysical properties using pumpout sampling data acquired with a wireline formation tester," *Proceedings of the Annual Technical Conference and Exhibition: Society of Petroleum Engineers*, Paper SPE 77345, San Antonio, Texas, Sep. 29–Oct. 2, 2002.
22. Zeybek, M., T. S. Ramakrishnan, S. S. Al-Otaibi, S. P. Salamy, and F. J. Kuchuk, "Estimating multiphase flow properties using pressure and flowline water-cut data from dual-packer formation tester interval tests and openhole array resistivity measurements," *Proceedings of the Annual Technical Conference and Exhibition: Society of Petroleum Engineers*, Paper SPE 71568, New Orleans, Lousiana, Sep. 30–Oct. 3, 2001.
23. Zhang, J.-H., Q. Hu, and Z.-H. Liu, "Estimation of true formation resistivity and water saturation with a time-lapse induction logging method," *The Log Analyst*, Vol. 40, No. 2, 138–148, 1999.
24. Alpak, F. O., C. Torres-Verdín, and T. M. Habashy, "Joint inversion of pressure and DC resistivity measurements acquired with in-situ permanent sensors: A numerical study," *Geophysics*, Vol. 69, No. 5, 1173–1191, 2004.
25. Alpak, F. O., C. Torres-Verdín, and T. M. Habashy, "Petrophysi-

cal inversion of borehole array-induction logs: Part I — Numerical examples," *Geophysics*, Vol. 71, No. 4, F101–F119, 2006.

26. Torres-Verdín, C., F. O. Alpak, and T. M. Habashy, "Petrophysical inversion of borehole array-induction logs: Part II — Field data examples," *Geophysics*, Vol. 71, No. 5, G261–G268, 2006.
27. Alpak, F. O., C. Torres-Verdín, and T. M. Habashy, "Estimation of in-situ petrophysical properties from wireline formation tester and induction logging measurements: A joint inversion approach," *Journal of Petroleum Science and Engineering*, Vol. 63, No. 1–4, 1–17, 2008.